ORNL/TM--9547

DE86 006767

ORNL/TM-9547
Dist. Category UC-20 g

FUSION ENERGY DIVISION

ORMEC: A THREE-DIMENSIONAL MHD SPECTRAL INVERSE EQUILIBRIUM CODE

S. P. Hirshman
J. T. Hogan

Date Published - February 1986

Prepared by the
OAK RIDGE NATIONAL LABORATORY
Oak Ridge, Tennessee 37831
operated by
MARTIN MARIETTA ENERGY SYSTEMS, INC.
for the
U.S. DEPARTMENT OF ENERGY
under Contract No. DE-AC05-84OR21400

CONTENTS

ABSTRACT

The Oak Ridge Moments Equilibrium Code (ORMEC) is an efficient computer code that has been developed to calculate three-dimensional MHD equilibria using the inverse spectral method. The fixed boundary formulation, which is based on a variational principle for the spectral coefficients (moments) of the cylindrical coordinates R and Z, is described and compared with the finite difference code BETA developed by Bauer, Betancourt, and Garabedian. Calculations for the Heliotron, Wendelstein VIIA, and Advanced Toroidal Facility (ATF) configurations are performed to establish the accuracy and mesh convergence properties for the spectral method.

1. INTRODUCTION

The accurate numerical determination of magnetohydrodynamic (MHD) equilibria in complex three-dimensional (3-D) geometries is an important aspect of the design and interpretation of thermonuclear confinement experiments. Plasma equilibria are required for stability, transport, and heating calculations, as well as for data analysis applications.

Recently, there has been considerable progress in the development of accurate and efficient spectral methods for computing 3-D equilibria using the inverse representation.[1-4] Common to all the spectral approaches is a Fourier expansion for the cylindrical coordinates (R,Z) in a toroidal domain:

$$R = \sum \left[R^c_{mn}\cos(m\theta - n\phi) + R^s_{mn}\sin(m\theta - n\phi)\right] ,$$

$$Z = \sum \left[Z^c_{mn}\cos(m\theta - n\phi) + Z^s_{mn}\sin(m\theta - n\phi)\right] . \qquad (1)$$

Here, θ is a poloidal angle, ϕ is the toroidal angle, and $\left[R_{mn}(s), Z_{mn}(s)\right]$ are the "moments" of (R,Z) that are determined by Fourier analysis of the components of the MHD force balance equation:

$$\vec{F} \equiv -\vec{J} \times \vec{B} + \nabla p = 0 . \qquad (2)$$

Here, $p = p(s)$ is the plasma pressure, and s labels a magnetic surface. The current is $\vec{J} = \nabla \times \vec{B}$. The following contravariant representation for the magnetic field $\vec{B}$ is used:

$$\vec{B} = \Phi'\left[\nabla s \times \nabla\theta - \iota\nabla s \times \nabla\phi + \nabla s \times \nabla\lambda\right] , \qquad (3)$$

where $\Phi'(s)$ is the toroidal flux derivative, $\iota(s)$ is the rotational transform, and $\lambda(s,\theta,\phi)$ is a stream function.

The various existing spectral codes differ primarily in three respects: (1) the choice of the angle θ, which is governed by the representation in Eq. (1) and by the function λ in Eq. (3); (2) the radial representation of the spectral equations; and (3) the numerical algorithm used for solving the nonlinear force equations to obtain the moment amplitudes. The Oak Ridge Moments Equilibrium Code (ORMEC) uses a pseudo-polar angular representation for R and Z and solves a linear equation for the radial current to obtain λ. Solutions for the spectral amplitudes of R, Z, and λ are obtained at discrete radial mesh points using a modified steepest-descent algorithm.

Since there is a dearth of published, well-documented numerical 3-D equilibria, we have chosen to benchmark ORMEC by running it concurrently with the BETA code.[5] Several confinement geometries, together with different plasma and magnetic parameters, have been considered. In this way, a data base of 3-D numerical results has been established that may also facilitate future code documentation.

Because BETA and ORMEC both perform the same energy minimization, the comparison undertaken here provides a sensitive test of the different numerical schemes used in these codes. BETA employs a finite difference version of the MHD equations. Thus, it provides a distinct measure of comparison for any spectral code. Convergence properties with respect to finite meshes differ in BETA and ORMEC, since spectral convergence in the mean is generally quite different from the pointwise convergence of finite differences. No mesh extrapolation scalings have heretofore been established for such physically important parameters as the shift or the elongation.

This report is organized as follows. In Sect. 2, a brief description of ORMEC is presented. The radial difference scheme and descent equations used in ORMEC are reviewed. In Sect. 3, the mesh and spectral convergence properties of the ORMEC code are established through the analysis of two-dimensional (2-D) equilibria. In Sect. 4, the various 3-D examples used to compare ORMEC with BETA are described

and the results of the equilibrium computations for varying shear and pressure profiles are presented. In Sect. 5, the mesh convergence of several physical quantities, the most important being the energy and the position of the magnetic axis, is compared for the spectral and finite difference methods.

The primary aim of this investigation is to establish the accuracy and convergence properties of the spectral equilibrium code ORMEC. Computational times are therefore not emphasized. Indeed, any comparison of CPU times for the spectral and finite difference codes is difficult to assess fairly, since different grids, etc., are used. Generally, the computational speed of the spectral code is competitive with (and typically at least two to three times faster than) the BETA code when a prescribed error tolerance must be satisfied.

2. ORMEC CODE DESCRIPTION

Both the spectral method and a preliminary version of ORMEC have previously been described.[1] Here, some of the main numerical features of the inverse spectral method are reviewed. New developments stimulated by experience with 3-D equilibrium computations are emphasized.

ORMEC solves a set of nonlinear elliptic partial differential equations describing MHD force balance by Fourier analysis of the inverse coordinates R and Z in terms of (θ,ζ), where (s,θ,ζ) are magnetic flux coordinates. This reduces the equilibrium equations to coupled, second-order ordinary differential equations for the moment expansion coefficients $[R_{mn}(s)$ and $Z_{mn}(s)$ in Eq. (1)$]$. The cylindrical coordinates R and Z are augmented by a stream function λ, defined in Eq. (3), which assumes the role of a renormalization parameter for accelerating the convergence of the series representation in Eq. (1). The stream function λ is determined by $\vec{J} \cdot \nabla s = 0$, which yields a linear elliptic equation for λ. However, this equation is in general a linear combination of the force equations determining R and Z. This leads to an underdetermined, or ill-conditioned, set of equations for the amplitudes of R, Z, and λ. A unique set of spectral equations results by imposing a set of constraints between the coefficients R_{mn} and Z_{mn}. In this way, the numerical convergence properties of the force balance equations are greatly improved. [In practice, the λ-augmented set of moment equations can become ill conditioned for poloidal mode numbers [m in Eq. (1)] as small as 2.

2.1 Poloidal Angle Selection

Several constraint relations between the R and Z Fourier coefficients have been suggested and used in the literature.[1-3,6] In the present version of ORMEC, a quasi-polar description[7] is used that defines a unique poloidal angle as follows:

$$R = \sum_{n=0}^{N} \left(R_{0n}^{c}\cos n\phi - R_{0n}^{s}\sin n\phi\right)$$

$$+ \sum_{n=-N}^{N} \left[R_{1n}^{c}\cos(\theta - n\phi) + R_{1n}^{s}\sin(\theta - n\phi)\right] + \bar{r}\cos\theta ,$$

$$Z = \sum_{n=0}^{N} \left(Z_{0n}^{c}\cos n\phi - Z_{0n}^{s}\sin n\phi\right)$$

$$+ \sum_{n=-N}^{N} \left[Z_{1n}^{c}\cos(\theta - n\phi) + Z_{1n}^{s}\sin(\theta - n\phi)\right] + \bar{r}\sin\theta ,$$

$$\bar{r} = \sum_{n=0}^{N} \left(r_{0n}^{c}\cos n\phi - r_{0n}^{s}\sin n\phi\right)$$

$$+ \sum_{n=-N}^{N} \sum_{m=3}^{M} \left[r_{mn}^{c}\cos(m\theta - n\phi) + r_{mn}^{s}\sin(m\theta - n\phi)\right] . \qquad (4)$$

Here, M and N are the maximum poloidal and toroidal mode numbers, respectively, and all the spectral amplitudes are functions of s. The m = 0 components of R and Z in Eq. (4) represent the axis of a polar system for each surface s = const, and the m = 1 components are constrained to satisfy $Z_{1n}^{c} = R_{1n}^{s}$ and $Z_{1n}^{s} = -R_{1n}^{c}$. (At s = 0, the curve described by the R_{0n} and Z_{0n} coefficients is the magnetic axis.) The m = 0 components of $\bar{r}$ combine with the R_{1n} terms of R and Z to yield ellipses that, in general, may rotate and deform as functions of ϕ. The remaining $m \geq 3$ terms that compose $\bar{r}$ represent perturbations of these elliptical shapes.

The constraint between R_{mn} and Z_{mn} in Eq. (4) removes the degeneracy in the (R,Z,λ) system of equations. Let F_R and F_Z be the MHD force components conjugate to R and Z, respectively, which have been previously computed in Ref. 1. The forces appearing in the

descent equations for R_{0n}, R_{1n}, Z_{0n}, and r_{mn} can then be obtained from the variational principle

$$\delta W = -\int (F_R \delta R + F_Z \delta Z) ds \, d\theta \, d\phi \tag{5}$$

by inserting the representation in Eq. (4) for δR and δZ into Eq. (5). The result is

$$\begin{aligned} F_j^{0n} &= \int F_j \exp(-in\phi) \, d\theta \, d\phi \, , \\ F_R^{1n} &= \int (F_R + iF_Z) \exp[i(\theta - n\phi)] d\theta \, d\phi \, , \\ F_r^{mn} &= \int (\cos\theta \, F_R + \sin\theta \, F_Z) \exp[i(m\theta - n\phi)] d\theta \, d\phi \, , \end{aligned} \tag{6}$$

where $F_j^{mn} = (F_j^{mn})_c + i(F_j^{mn})_s$ for $j = R$, Z, or $\bar{r}$. Let X_j^{mn} represent one of the moment amplitudes R_{0n}, R_{1n}, or r_{mn}, and let the conjugate force be denoted F_j^{mn}. Then the descent equation used in DRMEC to evolve X_j^{mn} is

$$\frac{d^2 X_j^{mn}}{dt^2} + \omega_d \frac{dX_j^{mn}}{dt} = F_j^{mn} \, . \tag{7}$$

Here, ω_d is a damping parameter chosen to approximate the time scale of the slowest decaying eigenmodes of F. The second-order time derivative appears in Eq. (7) to accelerate the temporal convergence of the descent equations when the operator F is stiff. The timestep Δt used to integrate Eq. (7) is estimated from the Courant-Friedrichs-Lewy condition $\Delta t \sim \Delta s / v_A$. Thus, Δt is the time for a wave moving at the Alfvén speed v_A to cross one radial mesh zone, Δs. To avoid unnecessarily long computations, it is desirable to choose Δt as large as possible. Since Δt can only be estimated, a numerical instability may be excited if the chosen Δt is too large. To suppress the

resulting rapid departure from force balance, ORMEC monitors the transformation Jacobian $\sqrt{g}$, reducing Δt automatically whenever $\sqrt{g}$ vanishes (except at the magnetic axis). This results in a very robust integration scheme that does not require elaborate initial timestep estimation.

2.2 Improved Radial Discretization

The radial discretization of F_R and F_Z used in ORMEC has been chosen to improve the accuracy of the finite difference representation of the forces that are computed on a fixed radial mesh. The discretization scheme was motivated by noting[1,5] that F_R and F_Z are linear combinations of F_s (the radial component of the force) and F_λ (the tangential force component). Thus, any radial differencing should be consistent with this decomposition and with the differencing used for F_λ. (This is particularly important when the quasi-polar representation is used, since F_r is a linear combination of F_R and F_Z.)

Three types of alterations have been made as compared with Ref. 1. Let X represent either R or Z. Then, the term

$$I \equiv \frac{\partial}{\partial s}\left(X_\theta P\right) - \frac{\partial}{\partial \theta}\left(X_s P\right) \tag{8a}$$

appearing in F_R and F_Z is differenced as follows on the integer radial mesh (excluding the origin, s = 0):

$$I^j = X^j_\theta \left(\frac{P^{j+1/2} - P^{j-1/2}}{\Delta s}\right) + \left(\frac{X^{j+1}_\theta - X^{j-1}_\theta}{2\Delta s}\right) P^j$$

$$- \frac{\partial}{\partial \theta}\left[\left(\frac{X^{j+1} - X^{j-1}}{2\Delta s}\right) P^j\right] , \tag{8b}$$

where

$$P^{j+1/2} = \frac{u^{j+1/2}}{2}\left(\frac{b^j + b^{j+1}}{2}\right) ,$$

$$P^j = \left(\frac{u^{j+1/2} + u^{j-1/2}}{2}\right) b^j .$$

Here, $u = (\Phi'/\tau)^2$ and $\tau = \sqrt{g}/R$ are differenced on a half-integral radial mesh, where $s_{j+1/2} \equiv (j - 1/2)\Delta s$, and $b = (\sqrt{g})^2|B|^2/R$ is differenced on the integral mesh for which $s_j = (j - 1)\Delta s$. Although Eq. (8b) is a numerically conservative form, the $X_s P$ term is now evaluated at s_j as a product of X_s^j and P^j, in contrast with the previous result where $X_s P$ was averaged over half-integer grid points.

The second type of change involves representing the quantity $\tilde{I} = (\Phi')^2/\tau$ on the integer mesh. Wherever $\tilde{I}$ appears in the expressions for F_R or F_Z, it is differenced as follows:

$$\tilde{I}^j = \frac{1}{2}\left(u^{j+1/2} + u^{j-1/2}\right)\left(R_\theta Z_s - R_s Z_\theta\right)^j . \qquad (8c)$$

The final change improves the asymptotic behavior of the Jacobian $(\sqrt{g})$ near the magnetic axis, $s = 0$. One should note that the moment coefficients in Eq. (4) have the expansions $R_{0n} = R_{0n}(0) + O(s^2)$, $Z_{0n} = Z_{0n}(0) + O(s^2)$, $R_{1n} \sim s$, $r_{0n} \sim s$, and $r_{mn} \leq s^2$ for $m \geq 3$, which are valid as $s \to 0$. Thus, the quantities R_θ and Z_θ evaluated at the first half-mesh point are not simply the average of their origin and first integer mesh values. For example, the $m = 2$ modes, which contribute to the origin forces, would be incorrectly represented this way. For $X = R$ or Z, the half-mesh values of X_θ are written correctly as follows:

$$X_\theta^{1/2} = \frac{1}{2} X_\theta^1 - \frac{1}{4} \bar{X}_\theta^1 , \qquad (9)$$

where $\bar{X}^1_\theta$ is the value of X_θ, excluding m = 1 harmonics, at the first integer mesh point from the origin.

The increased radial resolution resulting from these modifications is demonstrated in Sect. 3 by comparing several 2-D equilibria.

2.3 Zero-Current Algorithm

As an alternative to flux conservation, ORMEC includes an algorithm for finding the rotational transform profile $\iota(s)$ corresponding to an equilibrium with zero net toroidal current on each flux surface. The variation of the MHD energy W with respect to ι (keeping the toroidal flux, pressure, and surface topology fixed) yields

$$\delta W = \int \Phi' \langle j_\phi \rangle \delta\iota \, ds \, , \tag{10}$$

where $\langle j_\phi \rangle \equiv \int d\theta \, d\zeta \, \sqrt{g} \, \vec{J} \cdot \nabla\phi = (2\pi)^{-2} \partial \bar{B}_\theta / \partial s$, with

$$\bar{B}_\theta = (2\pi)^{-2} \int d\theta \, d\zeta \, B_\theta \, .$$

Here, $2\pi\bar{B}_\theta$ is the net toroidal current enclosed by a magnetic surface. The minimum energy state, therefore, corresponds to $\bar{B}_\theta = 0$ and may be obtained from a descent equation[8] of the form $d\iota/dt = -\Phi' \langle j_\phi \rangle$. In ORMEC, the zero current state is maintained throughout the computation by explicitly solving the linear equation $\bar{B}_\theta = 0$ for ι at each time step, yielding

$$\iota = \left\langle \frac{\Phi'}{\sqrt{g}} \left[\lambda_\zeta g_{\theta\theta} - (1 + \lambda_\theta) g_{\theta\zeta} \right] \right\rangle \Big/ \left\langle \frac{\Phi'}{\sqrt{g}} \, g_{\theta\theta} \right\rangle \, . \tag{11}$$

Thus, a nonzero value of ι can be obtained in a zero net toroidal current plasma only if there are helical distortions of the flux surfaces (otherwise, $\lambda_\zeta = g_{\theta\zeta} = 0$).

3. TWO-DIMENSIONAL EQUILIBRIA

In this section, several 2-D equilibria are presented to demonstrate the mesh convergence properties of ORMEC and the effects of improved radial differencing. The first example is the Solov'ev equilibrium,[9] with exact flux surfaces described by $\chi/2\pi \equiv s^2 = 2Z^2/5 + (R^2 - 16)^2/64$. Table I compares the relative error in the poloidal flux, $|\Delta\chi/\chi|$, where $\Delta\chi(s) = \max |\chi(s,\theta) - s^2|$ and $\chi(s,\theta)$ is the numerically computed value of χ, for the original and improved differencing schemes on a 20-point radial mesh using 9 poloidal modes. Both schemes yield $R(0) = 4.000$ for the magnetic axis. There is a significant reduction of the relative error for $s \leq 0.85$ with the improved scheme, especially near the magnetic axis. For both schemes, the infinite mesh value for the energy, W_∞, was estimated by using quadratic mesh extrapolation: $W = W_\infty + \alpha(\Delta s)^2$. The results agree well with the exact value for $\gamma = 0$, $W_e = 61.20852\ldots$. Similarly, the value of the elongation at the origin, $E(0)$, computed with the improved differencing is in good agreement with the exact value $E_e = \sqrt{10}/2 = 1.5811\ldots$. For the original scheme, $E(0)$ extrapolates linearly with Δs to the correct value.

The second example[10] demonstrates the radial mesh dependence of the energy, the magnetic axis, and the elongation for a high-beta, circular plasma. The plasma boundary is described by $(R - 2.576)^2 + Z^2 = 0.25$, and the equilibrium toroidal flux contours are shown in Fig. 1. (The contours were, however, computed on an equally spaced $\sqrt{\chi}$ mesh.) The pressure profile $p(\chi) = 0.25(1 - \hat{\chi})^2$ was fixed ($\gamma = 0$), the q profile is $q(\chi) = [2/(4 - 3\hat{\chi})^{1/2}]1.325$, where $\hat{\chi} = s^2$ for $s \in (0,1)$, and the actual poloidal flux is $\chi/2\pi = 0.0758\,\hat{\chi}$. The volume-average beta, $\langle\beta\rangle$, was computed to be 0.205, compared with 0.196 obtained in Ref. 10. A total of eight Fourier amplitudes ($m \leq 7$) was retained. From Table II, note that the extrapolated values for the energy, magnetic axis position, and elongation (the latter evaluated at $\hat{\chi} = 0.1$) are nearly identical for the original and improved differencing schemes, and they are in excellent agreement with those in Ref. 10. The value of $R(0)$ [$E(0.1)$] converges to its infinite mesh

TABLE I

Effect of improved radial differencing on Solov'ev equilibrium

ORIGINAL DIFFERENCING			IMPROVED DIFFERENCING	
s	χ	$\lvert\Delta\chi/\chi\rvert$	χ	$\lvert\Delta\chi/\chi\rvert$
$5.00\cdot10^{-2}$	$2.50\cdot10^{-3}$	$2.22\cdot10^{-2}$	$2.50\cdot10^{-3}$	$5.96\cdot10^{-4}$
$1.00\cdot10^{-1}$	$1.00\cdot10^{-2}$	$1.84\cdot10^{-2}$	$1.00\cdot10^{-2}$	$3\ 40\cdot10^{-4}$
$2.00\cdot10^{-1}$	$4.00\cdot10^{-2}$	$1.23\cdot10^{-2}$	$4.00\cdot10^{-2}$	$5.14\cdot10^{-4}$
$3.00\cdot10^{-1}$	$9.00\cdot10^{-2}$	$8.06\cdot10^{-3}$	$9.00\cdot10^{-2}$	$5.01\cdot10^{-4}$
$4.00\cdot10^{-1}$	$1.60\cdot10^{-1}$	$5.13\cdot10^{-3}$	$1.60\cdot10^{-1}$	$3.99\cdot10^{-4}$
$5.00\cdot10^{-1}$	$2.50\cdot10^{-1}$	$3.10\cdot10^{-3}$	$2.50\cdot10^{-1}$	$2.87\cdot10^{-4}$
$6.00\cdot10^{-1}$	$3.60\cdot10^{-1}$	$1.91\cdot10^{-3}$	$3.60\cdot10^{-1}$	$2.30\cdot10^{-4}$
$7.00\cdot10^{-1}$	$4.90\cdot10^{-1}$	$1.07\cdot10^{-3}$	$4.90\cdot10^{-1}$	$1.81\cdot10^{-4}$
$8.00\cdot10^{-1}$	$6.40\cdot10^{-1}$	$5.05\cdot10^{-4}$	$6.40\cdot10^{-1}$	$1.25\cdot10^{-4}$
$9.00\cdot10^{-1}$	$8.10\cdot10^{-1}$	$1.94\cdot10^{-4}$	$8.10\cdot10^{-1}$	$8.60\cdot10^{-5}$
1.00	1.00	$1.02\cdot10^{-6}$	1.00	$1.02\cdot10^{-8}$
		$\Delta s = 0.05$		
61.19005		W	61.19006	
1.617		E(0)	1.581	
		$\Delta s = 0.04$		
61.196707		W	61.196712	
1.611		E(0)	1.581	
		$\Delta s = 0.033$		
61.20032		W	61.20032	
1.606		E(0)	1.581	
61.20853		W_∞	61.20853	
1.595(1.581)		E_∞	1.581	

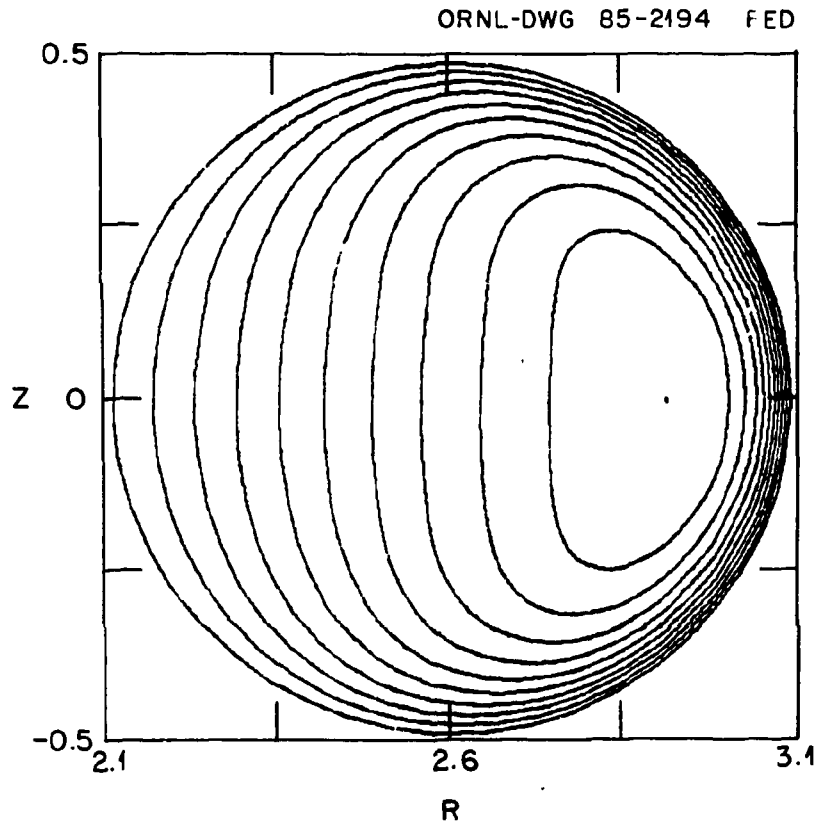

Fig. 1. Toroidal flux contours for a high-β, circular plasma.

value slightly faster using the improved (original) differencing, whereas the nonvariational radial force residual in the vicinity of the magnetic axis, $F_s(0)$, is considerably smaller for the improved scheme (which correctly treats the asymptotic behavior of $\sqrt{g}$ near the axis). Since the original radial differencing scheme is close to the one used in BETA[5] (see Sect. 4), this may clarify discrepancies between ORMEC and BETA that occur near the magnetic axis.

Figure 2 shows the decrease of the rms error in the radial force balance as a function of increasing poloidal mode number. When too few modes are retained, the D-shapes of the flux surfaces shown in Fig. 1 are poorly represented, leading to a large deviation from force balance. The sensitivity of this rms error to the mode number spectrum is useful for assessing the convergence (with respect to mode number) of both 2-D and 3-D equilibria.

TABLE II

Comparison of radial differencing schemes
for high beta circular plasma

ORIGINAL DIFFERENCING		IMPROVED DIFFERENCING
	$\Delta s = 0.05$	
4.085486	W	4.085575
2.886	R(0)	2.889
1.938	E(0.1)	1.899
0.57	$F_s(0)$	0.012
	$\Delta s = 0.04$	
4.091361	W	4.091410
2.889	R(0)	2.892
1.975	E(0.1)	1.945
0.68	$F_s(0)$	0.017
	$\Delta s = 0.033$	
4.094580	W	4.094610
2.892	R(0)	2.894
2.001	E(0.1)	1.979
0.76	$F_s(0)$	0.02
4.101896	W_∞	4.101883
2.899	R_∞	2.899
2.060	E_∞	2.056

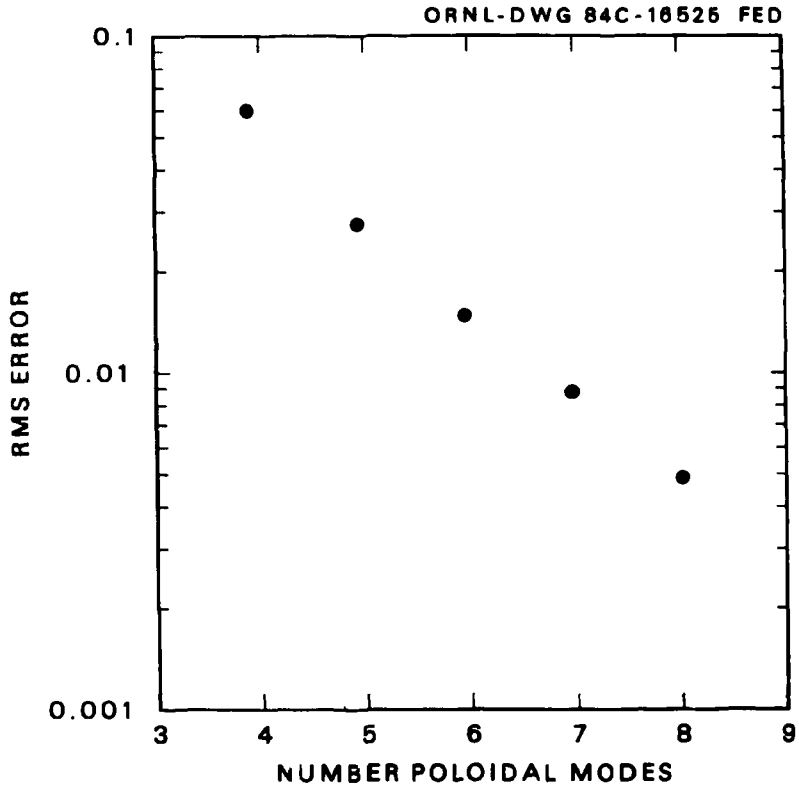

Fig. 2. rms error in radial force F_s vs number of poloidal harmonics, m, retained in series for R, Z, and λ.

4. COMPARISON WITH BETA RESULTS: TEST CASES

In this section, several 3-D equilibria are described that are subsequently used to compare the ORMEC and BETA codes. Only fixed boundary cases were analyzed. Although BETA is a free boundary code with a fixed boundary option, ORMEC has not yet been extended to solve free boundary problems. Thus, the parameter NVAC in BETA, which controls the vacuum computation, was always negative to provide a fixed plasma boundary.

Two versions of the BETA code have been used. One is essentially that described in Ref. 5, with the addition of a zero current algorithm.[8] The other version[11] embodies an improved differencing scheme for the radial force equation. While the newer BETA code is preferable in terms of computational efficiency, the older version was used for most of the comparisons since the bulk of previously published results has been obtained with this version. (Results are close for the two versions.)

4.1 Parameter Selection in the BETA Code

For the configurations considered here, the cylindrical coordinates of the assumed perfectly conducting wall have the form[5]

$$R(u,v) = \epsilon^{-1} + r_b \cos u - \Delta_2 \cos(u - v) ,$$

$$Z(u,v) = r_b \sin u + \Delta_2 \sin(u - v) , \qquad (12)$$

where u is a poloidal variable, $v = Q_L\phi$ is the geometric toroidal angle, Q_L is the number of field periods, and

$$r_b = 1 - \Delta_3 \cos(3u - v) . \qquad (13)$$

Here, ϵ^{-1} is the aspect ratio, and Δ_2 and Δ_3 are constants that respectively determine the helical ellipticity and D-shape of the

boundary. We note that the poloidal angle variable u is generally not the same as θ given by the quasi-polar representation in Eq. (4).

When BETA is run in the flux-conserving mode, the initial pressure and iota profiles are specified functions of the radial coordinate $\hat{R}(s)$:

$$p = p_0(1 - \hat{R}^2) ,$$
$$\iota = \iota_0 + \iota_2\hat{R}^2 . \tag{14}$$

For all the computations considered here, $\hat{R}^2 = \Phi(s)/\Phi(1) \equiv \hat{\Phi}(s)$ is the normalized toroidal flux. The pressure profile is related to the mass by the adiabatic relation

$$m(s) = p(s)\left(\frac{V'}{\hat{\Phi}'}\right)^{\gamma} , \tag{15}$$

where $V' = \iint du\, dv\sqrt{g}$, $\hat{\Phi}' = d\hat{\Phi}/ds$, and $\gamma = 2$ was chosen. Equations (14) and (15) are used to initialize m(s), which is then fixed during the energy minimization.

When the zero toroidal current option[8] is used, the iota profile is determined numerically from the highest resolution case of a mesh convergence sequence. A spline approximation is then used to translate this ι profile to coarser grids in the sequence. The algorithm used in BETA to obtain the net zero current state is

$$a_\mu \frac{d^2\iota}{dt^2} + e_\mu \frac{d\iota}{dt} = -I_t(s) . \tag{16}$$

Here, $I_t(s)$ is the total toroidal current inside the flux surface labeled by s, and the acceleration (a_μ) and descent (e_μ) coefficients are chosen to be $a_\mu = 0$ and $e_\mu = 1$, respectively. The iota profile

obtained from the steady-state solution of Eq. (16) should agree, on an infinite mesh, with that determined in the ORMEC code by Eq. (11).

4.2 Grid Selection

The choice of the radial mesh point distribution is important since convergence properties depend sensitively on it. In BETA, the radial zoning parameter α relates the flux surface label s to the normalized toroidal flux $\hat{\Phi}$ through the relation $s^{2\alpha} = \hat{\Phi}$. The choice $\alpha = 0.5$, corresponding to zoning equally spaced in the toroidal flux, was made for the present comparison.

Poor convergence of the magnetic axis and helical axis has been previously reported[3] using $\alpha = 1$ corresponding to $\sqrt{\hat{\Phi}}$ radial zoning. In the following, the axis shift $\Delta(0)$ is the distance between the mean position of the magnetic axis and the mean geometric center of the boundary flux surface. The helical shift Δ_1^{axis} is the $n = Q_L$ toroidal harmonic amplitude of the magnetic axis. Using the Heliotron configuration described in Ref. 3, we have investigated the dependence on α of the convergence rates for $\Delta(0)$ and Δ_1^{axis}. As seen from Table III, there is a substantial change in $\Delta(0)$ for $\alpha = 1.0$ in going from 7×12^2 to 13×24^2 grids. However, the $\alpha = 0.5$ sequence shows improved convergence properties. This motivates using $\alpha = 0.5$ in BETA (toroidal flux zoning) for the comparison with ORMEC.

Isotropic grids, $N \times N \times N$ in (s,θ,ζ), were chosen.[12] This defines a trajectory for the convergence sequence that will differ from that obtained previously[5] using BETA. The finest grid used for this study was $N^3 = 30^3$. The convergence study consists of results at grids of 15^3, 20^3, 25^3, and 30^3 points. While the energy is found to vary quadratically with the grid size, no definite convergence laws for other physical quantities (e.g., shift and helical axis amplitude) have been established.

In contrast, the 3-D extrapolations for ORMEC were performed on fixed poloidal and toroidal mode number grids. Only the radial grid size was varied. The number of harmonics was chosen large enough to achieve a prescribed error tolerance (typically, less than 1%) in the radial force balance. The different grid selections used for BETA and

TABLE III

Convergence dependence on radial zoning

GRID	α	$\Delta(0)$	Δ_1^{axis}
7×12^2	0.5	0.066	0.009
7×12^2	1.0	0.026	0.034
13×12^2	0.5	0.066	0.013
13×12^2	0.75	0.053	0.022
13×12^2	1.0	0.038	0.030
*13×24^2	1.0	0.033	0.036
13×24^2	0.75	0.050	0.025
13×24^2	0.5	0.065	0.016

*Case reported in Ref. 3.

ORMEC account in part for the different mesh scalings reported in the following Sections.

4.3 Test Cases

Three configurations were chosen for the comparison between ORMEC and BETA to demonstrate the effects of shear, aspect ratio, boundary shape and pressure on plasma equilibria:

1. W7A. The Wendelstein VIIA (W7A) configuration was chosen to reproduce its vacuum solution and to compare with an earlier study.[13] This is a low-shear, large-aspect-ratio device.

2. Heliotron (vacuum and high-beta). This is a fixed boundary version of the Heliotron configuration discussed in Ref. 14. The aspect ratio is intermediate between W7A and ATF. Stable equilibria at relatively high values of beta have been reported.

3. ATF (vacuum and high-beta). This is a simplified approximation to the ATF boundary,[15] and results have been published for BETA in

Ref. 11 using this approximation. This is the lowest aspect ratio case under study at present, and high-beta equilibria have been found for it. The shear is intermediate between Heliotron and W7A, although the ATF has the largest transform per field period of the three devices considered here.

The parameters characterizing the boundary for these cases are summarized in Table IV. For all cases, the iota profile was obtained from a 30^3 grid-size BETA run using the zero current constraint. The resulting mass and rotational transform profiles are shown in Figs. 3-7. [Note that $m/(2\pi^2)^2$ is plotted.] Also shown is the polynomial fit to the profiles obtained for each case from the high-resolution run. These curves were fitted with the series $\Sigma\, a_n \Phi^n$. The polynomial coefficients for the iota and mass profiles are given in Tables V and VI, respectively.

The equilibrium flux surfaces corresponding to the profiles in Figs. 3-7 are shown in Figs. 8-12. The surfaces are equally spaced in the toroidal flux, Φ, and were computed on a 30-point radial grid using ORMEC. The corresponding surfaces obtained from the finest 30^3 BETA grids are virtually indistinguishable for all cases. (The small differences in several geometric quantities are shown in Figs. 3-

TABLE IV

Parameters for test cases

CASE	Q_L	ϵ	Δ_2	Δ_3
1. W7A Vacuum	5	0.05	0.35	0.0
2. Heliotron	18	0.10	0.30	0.0
3. ATF	12	0.14	0.25	0.05

Q_L: Number of field periods.
ϵ: Inverse aspect ratio
Δ_i: Helical amplitudes defined in Eqs. (12) and (13).

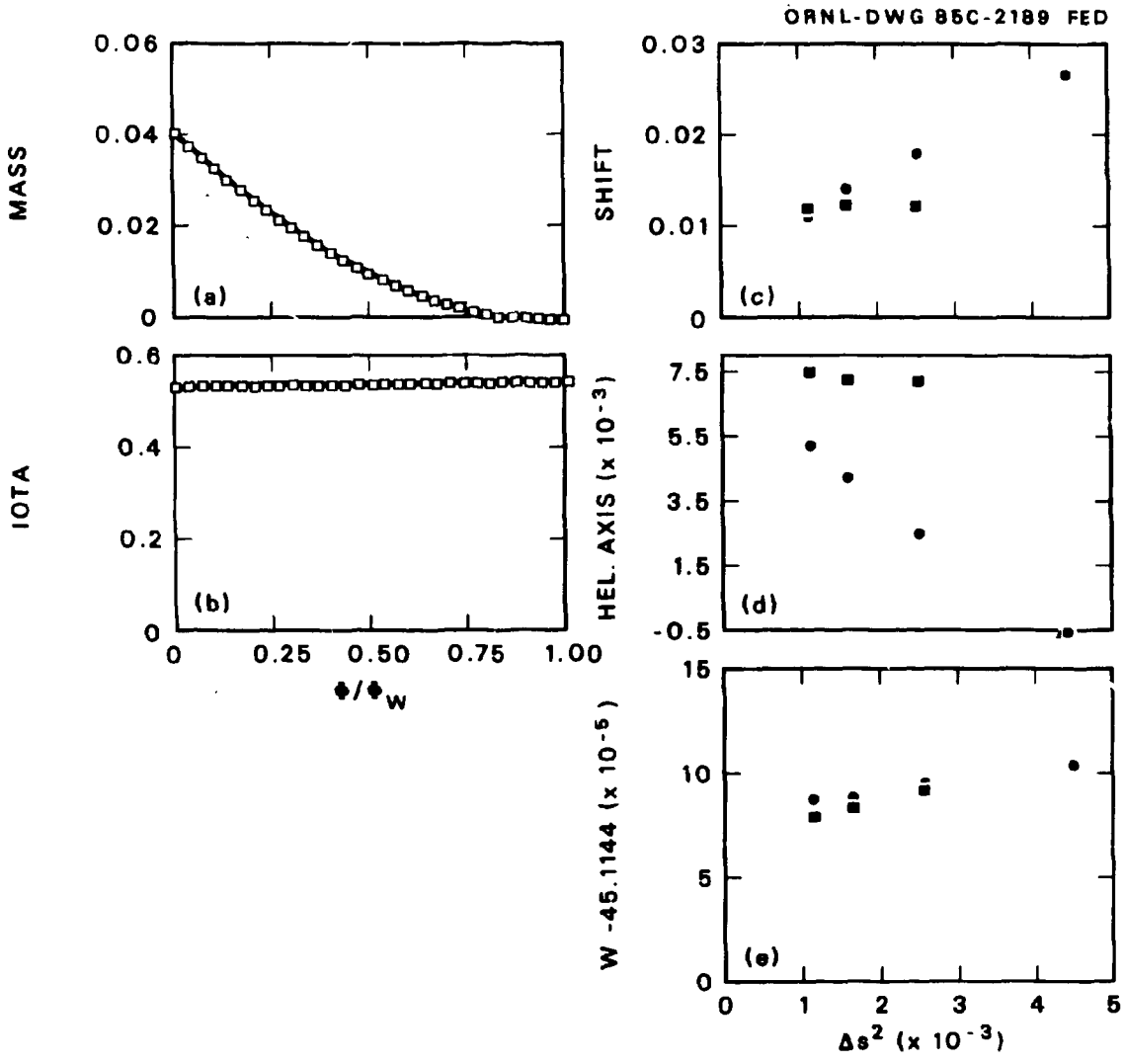

Fig. 3. W7A vacuum profiles and radial convergence studies. (a) Mass profile (open boxes are obtained from BETA on a 30^3 grid, and the curve is a spline fit); (b) Zero current profile; (c) Axis shift $\Delta(0)$ (solid circles are BETA data, solid boxes are ORMEC data); (d) Helical axis shift Δ_1^{axis}; and (e) equilibrium MHD energy, W.

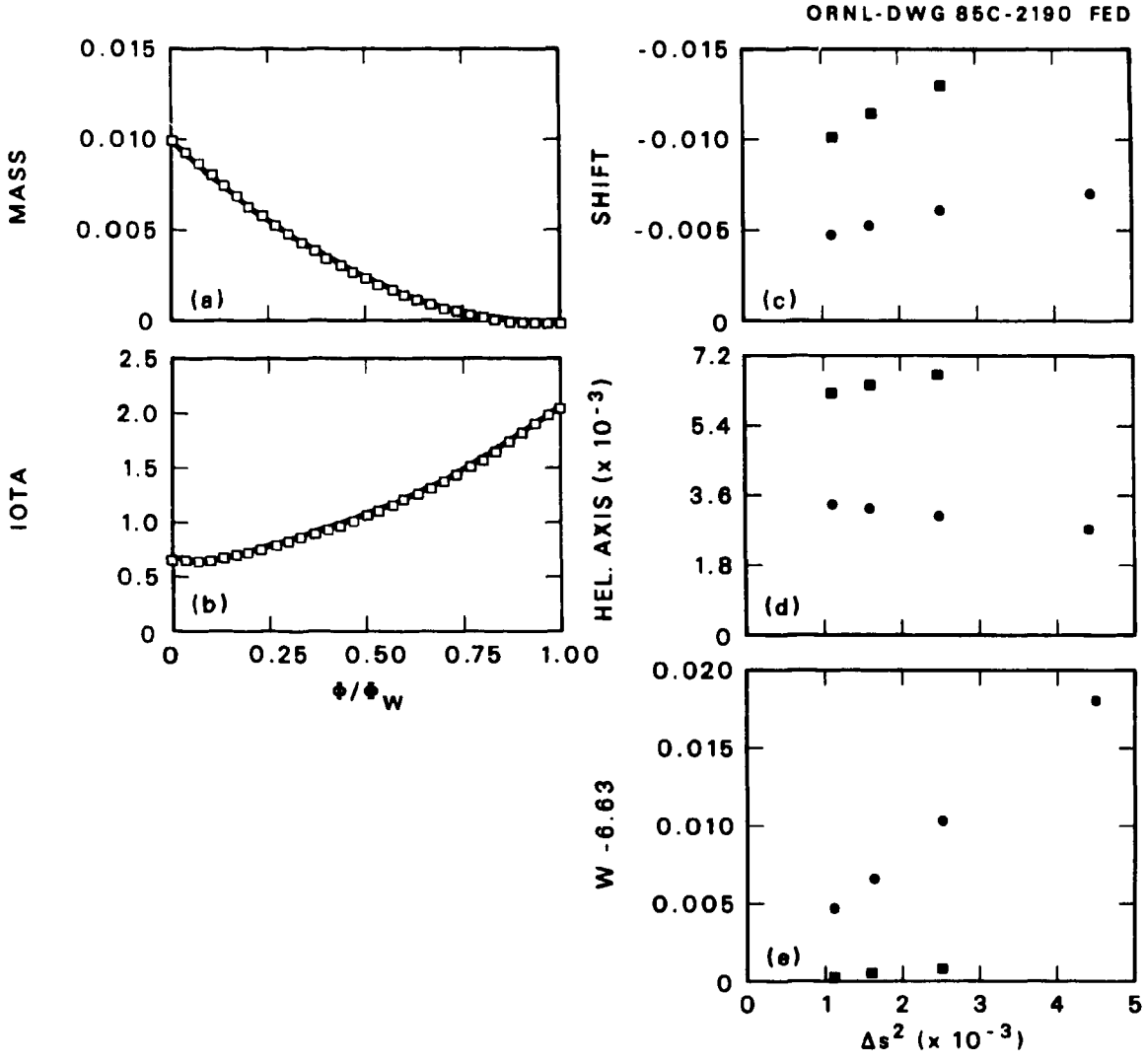

Fig. 4. Vacuum heliotron profiles and radial convergence studies (solid circles are BETA data and solid boxes are ORMEC data).

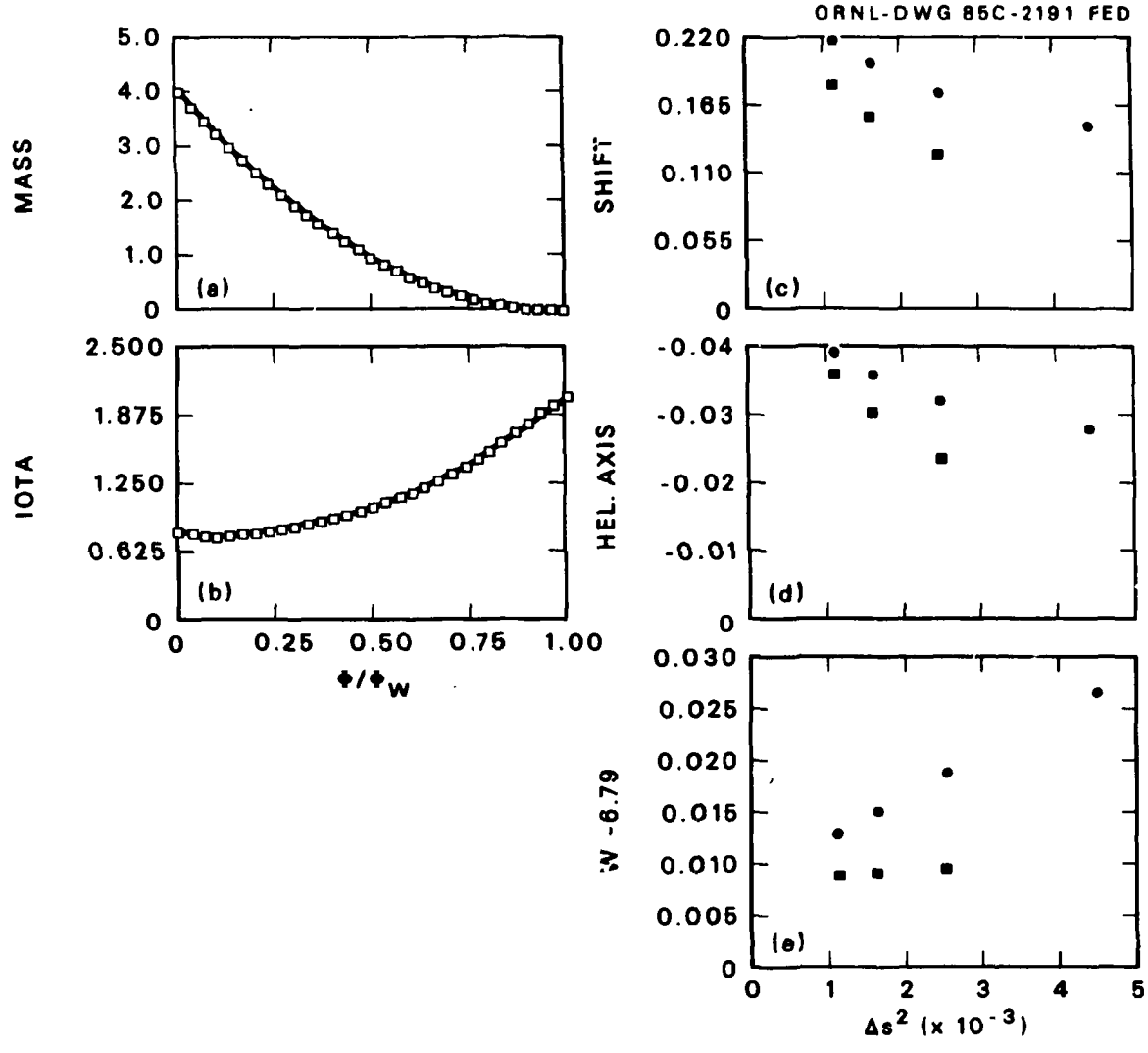

Fig. 5. High-β Heliotron profiles and radial convergence studies (solid circles are BETA data and solid boxes are ORMEC data).

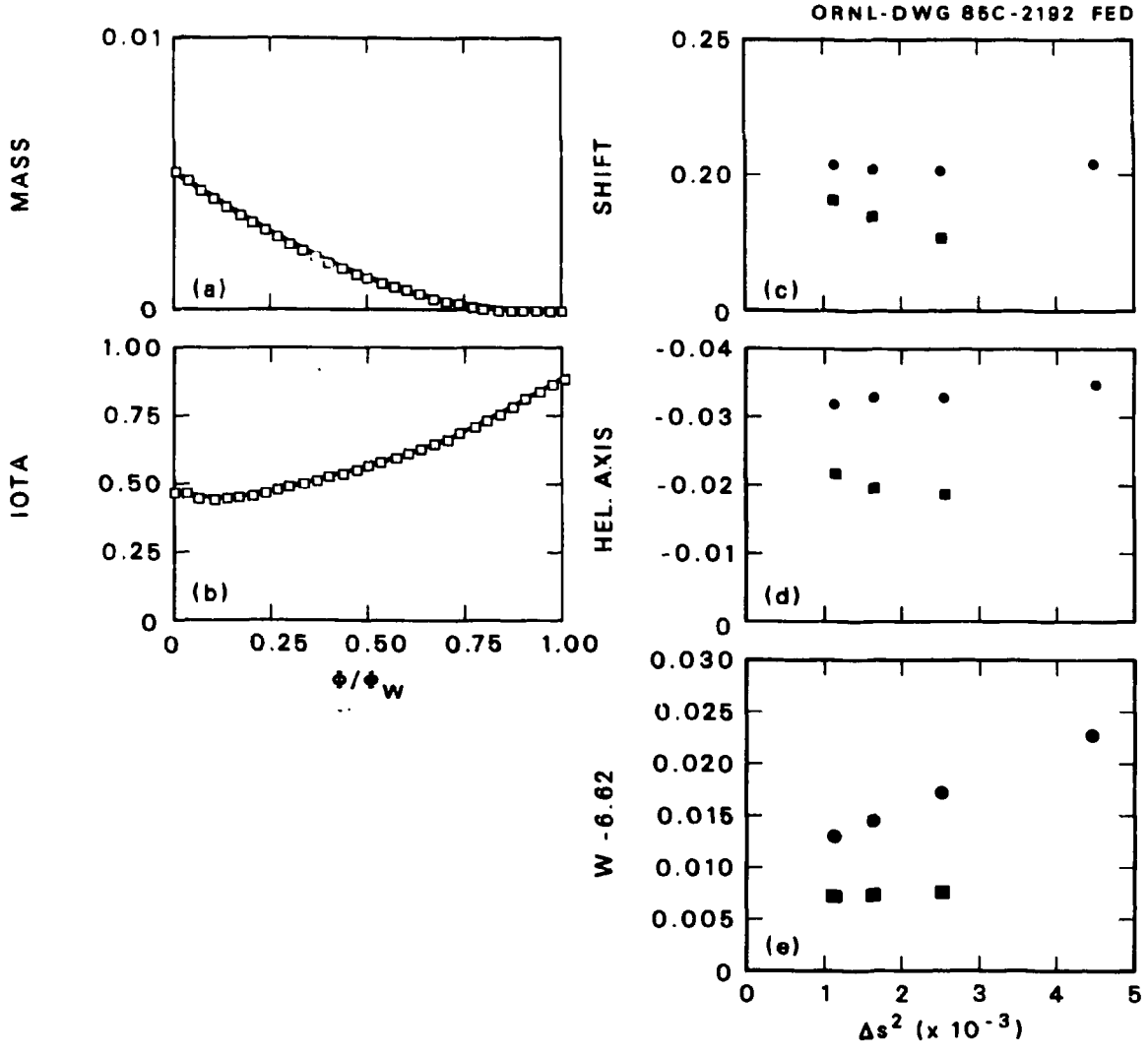

Fig. 6. Vacuum ATF profiles and radial convergence studies (solid circles are BETA data and solid boxes are ORMEC data).

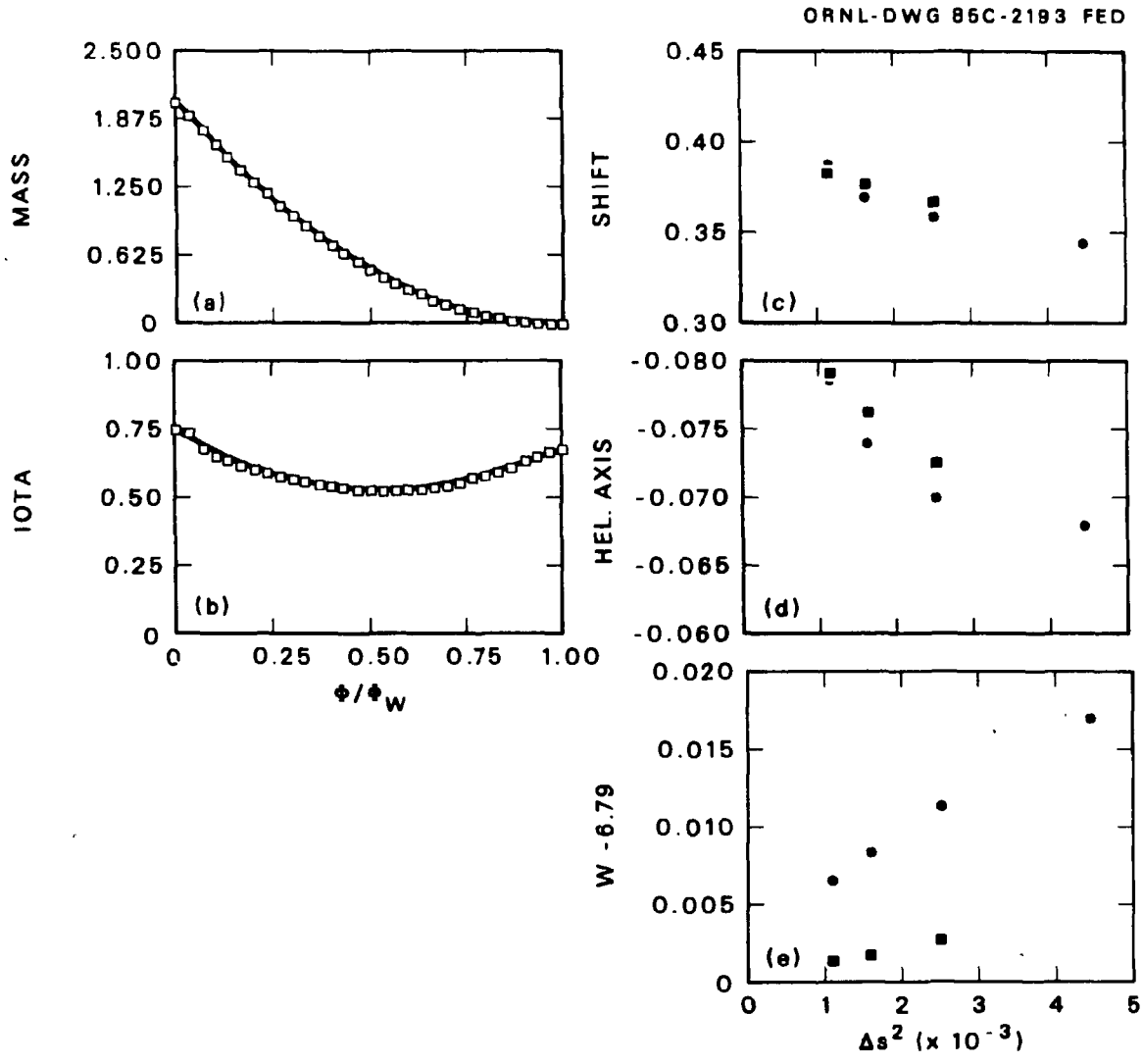

Fig. 7. High-β ATF profiles and radial convergence studies (solid circles are BETA data and solid boxes are ORMEC data).

TABLE V

Coefficients in the series $\iota = \sum_{j=1}^{N} a_j \hat{\phi}^j$

	W7A Vacuum	Vacuum Heliotron	High-β Heliotron	Vacuum ATF	High-β ATF
a_1	$5.318 \cdot 10^{-1}$	$6.606 \cdot 10^{-1}$	$8.015 \cdot 10^{-1}$	$4.687 \cdot 10^{-1}$	$7.563 \cdot 10^{-1}$
a_2	$6.335 \cdot 10^{-2}$	$-6.734 \cdot 10^{-1}$	-1.170	$-5.524 \cdot 10^{-1}$	-1.230
a_3	$-3.787 \cdot 10^{-1}$	7.572	9.892	3.721	2.720
a_4	1.531	$-1.565 \cdot 10^{1}$	$-3.184 \cdot 10^{1}$	-7.458	$-8.839 \cdot 10^{-1}$
a_5	-3.384	$1.606 \cdot 10^{1}$	$6.394 \cdot 10^{1}$	7.353	$-1.059 \cdot 10^{1}$
a_6	4.146	-5.88	$-7.395 \cdot 10^{1}$	-2.632	$2.301 \cdot 10^{1}$
a_7	-2.637	—	$4.759 \cdot 10^{1}$	—	$-1.806 \cdot 10^{1}$
a_8	$6.786 \cdot 10^{-1}$	—	$-1.320 \cdot 10^{1}$	—	4.916

TABLE VI

Coefficients in the Series $m = (2\pi^2)^2 \sum_{j=1}^{N} b_j \hat{\phi}^j$

	W7A Vacuum	Vacuum Heliotron	High-β Heliotron	Vacuum ATF	High-β ATF
b_1	$4.002 \cdot 10^{-2}$	$9.998 \cdot 10^{-3}$	4.001	$5.101 \cdot 10^{-3}$	2.042
b_2	$-7.833 \cdot 10^{-2}$	$-1.999 \cdot 10^{-2}$	-8.086	$-1.025 \cdot 10^{-2}$	-4.108
b_3	$1.577 \cdot 10^{-2}$	$1.000 \cdot 10^{-2}$	5.012	$5.470 \cdot 10^{-3}$	2.420
b_4	$1.064 \cdot 10^{-1}$	$-4.341 \cdot 10^{-5}$	-5.036	$-9.774 \cdot 10^{-4}$	-1.841
b_5	$-2.156 \cdot 10^{-1}$	$6.883 \cdot 10^{-5}$	$1.266 \cdot 10^{1}$	$1.037 \cdot 10^{-3}$	4.083
b_6	$2.238 \cdot 10^{-1}$	$-2.994 \cdot 10^{-5}$	$-1.685 \cdot 10^{1}$	$-3.853 \cdot 10^{-4}$	-4.539
b_7	$-1.152 \cdot 10^{-1}$	—	$1.132 \cdot 10^{1}$	—	2.440
b_8	$2.322 \cdot 10^{-2}$	—	-3.025	—	$-4.954 \cdot 10^{-1}$

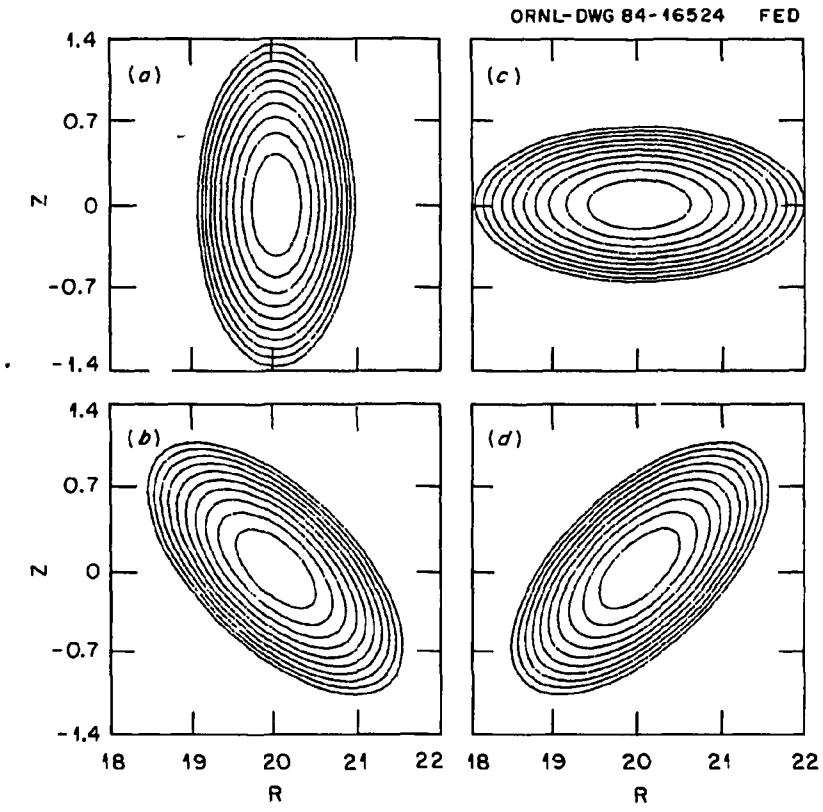

Fig. 8. W7A vacuum flux surfaces.

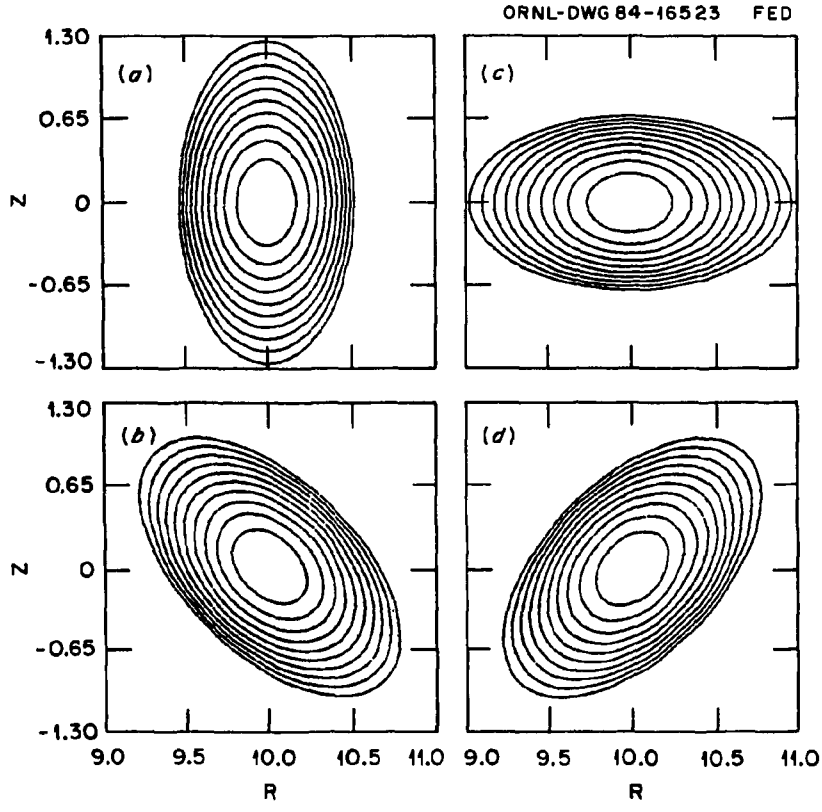

Fig. 9. Heliotron vacuum flux surfaces.

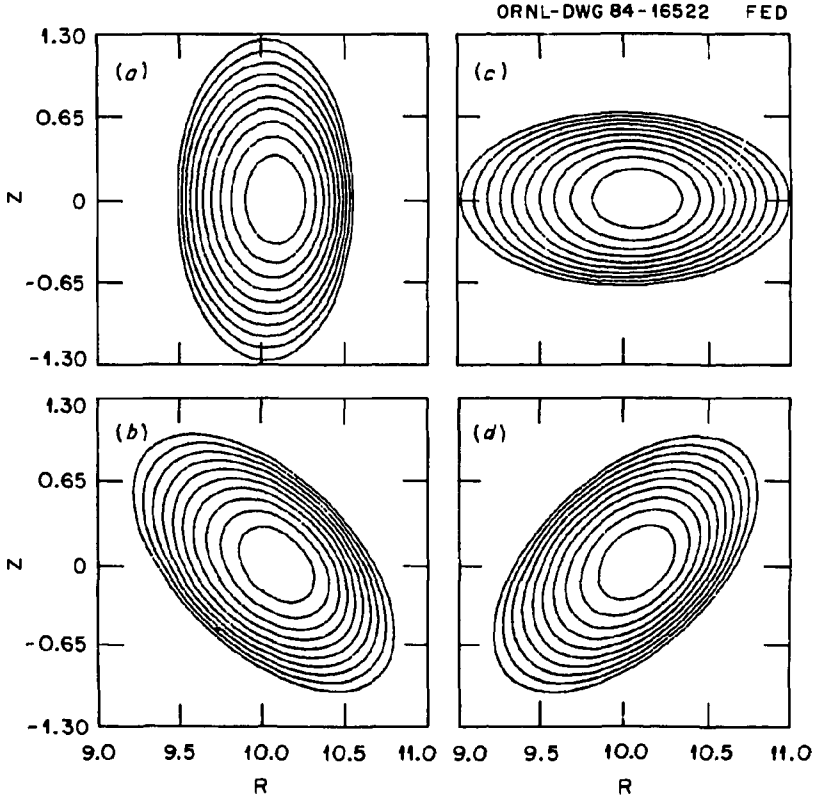

Fig. 10. Heliotron high-β flux surfaces.

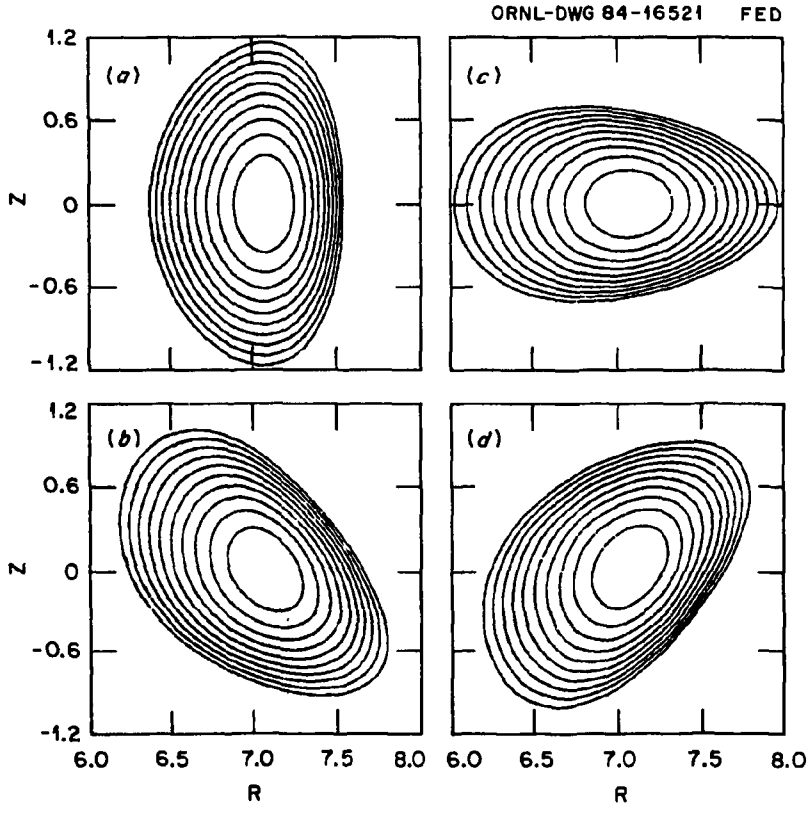

Fig. 11. ATF vacuum flux surfaces.

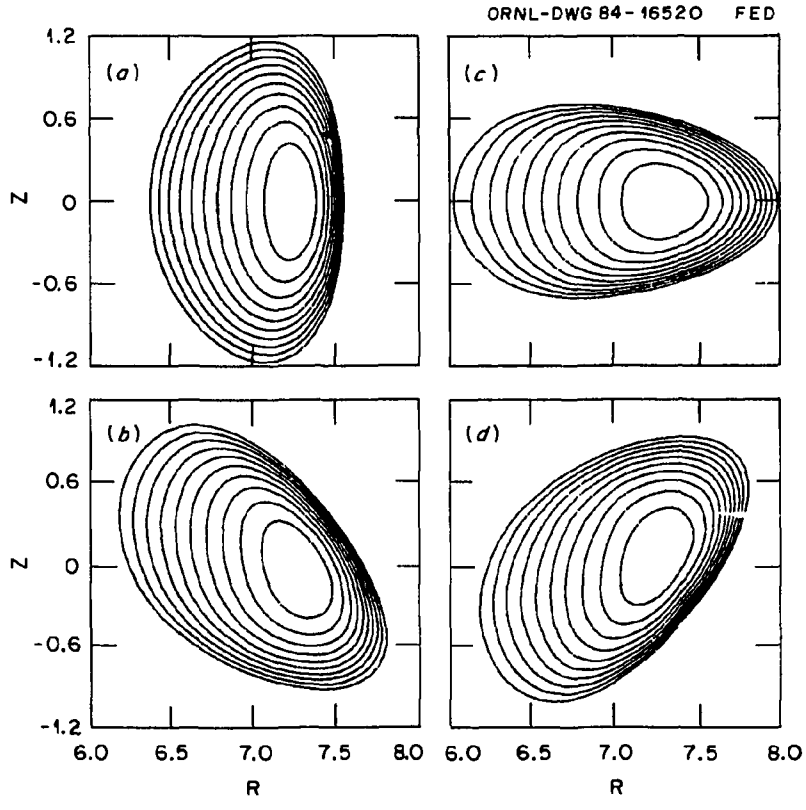

Fig. 12. ATF high-β flux surfaces.

5. RESULTS OF THE COMPARISON

The results of the ORMEC-BETA comparison are now presented for the various configurations introduced in Sect. 4. In all cases, a 6 x 6 mode-number spectrum was used in ORMEC [$m = 0, \ldots, 5$, $n = -2Q_L, 3Q_L$ in Eq. (4)], and Fourier transforms were computed on a 15 x 12 ($\theta - \phi$) angular mesh.

The results, which are discussed in detail in the following paragraphs and are tabulated in the Appendix, indicate nearly quadratic convergence with Δs for such quantities as the axis shift, helical shift, and energy computed from the ORMEC code. Except for the vacuum case, when the shifts are small (the BETA scalings being difficult to assess in this case), there is good agreement in these gross equilibrium features between the two codes. Discrepancies seem to increase as the boundary shape becomes more complex.

5.1 Wendelstein VIIA

The W7A vacuum case illustrates the complexities associated with the zero current algorithm. For a sequence during which ι is fixed at its value obtained from the finest grid (and subsequently interpolated to the coarser meshes), the convergence of the shift and energy is shown in Table A.1. The extrapolated values are obtained using quadratic extrapolation from the 25^3 and 30^3 cases. The shift $\Delta(0)$ decreases as the grid is refined, while there is a divergence away from the analytical result[16] $\Delta_1^{axis} = 0$ for the helical axis shift. The analytic result for the shift is $\Delta(0) = 0.04$, which is valid for $\epsilon Q_L \ll 1$. Since $\epsilon Q_L = 0.25$ in this case, the second-order correction is comparable to the leading-order term, and the discrepancy between BETA and ORMEC results for $\Delta(0)$ cannot be resolved using the lowest-order analytic predictions.

In contrast, when the zero current option is used on each grid (thus allowing ι to vary), the helical axis shift decreases monotonically as the mesh is refined. For the finest grid, ι approaches the value used to obtain the results in Table A.1. Table VII shows the shifts and energy for this convergence sequence. Thus, two different

TABLE VII

BETA results for W7A vacuum case with variable ι and zero current

Grid	$\Delta(0)$	Δ_1^{axis}	W
20^3	-.0015	.0092	45.11453
30^3	.011	.0052	45.11449
Extrapolated	.021	.0020	45.11448

extrapolation sequences (flux-conserving vs zero current) yield different values for $\Delta(0)$ and Δ_1^{axis} using the BETA code.

The results from ORMEC for this case when ι is fixed are also given in Table A.1. The ORMEC results are quite close to the finest resolution BETA results even at a coarser radial grid size. This is despite the fact that the extrapolated values for $\Delta(0)$ are different.

As seen in Fig. 3(c and d), the convergence properties are quite dissimilar for the shift and helical axis amplitude obtained from BETA. The shift appears to scale linearly with Δs, while the helical axis amplitude appears to be proportional to Δs^{-1}. The ORMEC results, however, depend only very weakly on the radial spacing. Thus, the extrapolated BETA results for $\Delta(0)$ and Δ_1^{axis} are sensitive to the assumed extrapolation law, and this may account for part of the discrepancy between the ORMEC and BETA predictions. In contrast, the final energy is expected to vary quadratically with Δs in both cases. The energy convergence is shown in Fig. 3(e). The ORMEC- and BETA-extrapolated energies agree to six significant figures.

The BETA results obtained here differ from those in Ref. 13. While the results in Ref. 13 correspond to a Gaussian pressure profile,

this is not sufficient to explain the discrepancy. It is likely that the difference is due to the choice of the radial zoning parameter α.

5.2 Heliotron

Vacuum Case

Heliotron has $\epsilon Q_L = 1.8$, so that the vacuum analytic shift results are not valid. The scaling of energy with grid size is clearly quadratic for both BETA and ORMEC [Fig. 4(e) and Table A.2], with a relative discrepancy $\delta W/W^{BETA} = 2 \times 10^{-5}$. The shift and the helical axis amplitudes are shown in Fig. 4(c and d). The mesh scaling is nearly linear in Δs^2 for all quantities and for both codes.

High-Beta Case

For the high-beta case, the axis value of beta, β_0, is 0.077, with $\langle\beta\rangle_{BETA} = 0.0249$ and $\langle\beta\rangle_{ORMEC} = 0.0251$. The energy convergence is quadratic. As seen in Fig. 5(e) and Table A.3, the ORMEC and BETA values for W are close: $\delta W/W^{BETA} = 2 \times 10^{-5}$.

The extrapolated shift and helical axis results [Fig. 5(c and d)] deviate by less than 10%, and quadratic mesh convergence for the ORMEC data is apparent.

5.3 ATF

Vacuum Case

The energy converges quadratically for the ATF vacuum case, with a relative discrepancy between BETA and ORMEC of $\delta W/W^{BETA} = 3.7 \times 10^{-4}$ [Fig. 6(e) and Table A.4]. The extrapolated shift and helical axis values agree to within better than 10% [Fig. 6(c and d)].

High-Beta Case

The high-beta ATF case for which $\beta_0 = 0.07$ (with $\langle\beta\rangle_{BETA} = 0.0245$ and $\langle\beta\rangle_{ORMEC} = 0.0243$) exhibits quadratic energy convergence [Fig. 7(e) and Table A.5] with a discrepancy $\delta W/W^{BETA} = 3.2 \times 10^{-4}$. As for the vacuum case, the extrapolated shift and helical axis values for both

codes are in good agreement [Fig. 7(c and d)], with the ORMEC data once again exhibiting quadratic mesh scaling.

Note that the energy deviation $\delta W/W^{BETA}$ is an order of magnitude larger for ATF than for either Heliotron or W7A (although it is still quite small). Because of the nonzero value of Δ_3, the ATF boundary has additional complexity compared with the elliptical cases. Thus, discrepancies between different codes seem to be enhanced for more complex boundaries, an effect that is related to angular grid resolution of the boundary.

The boundary complexity, together with finite beta, has a significant influence on the poloidal harmonic spectrum required in ORMEC to yield an approximate equilibrium with an acceptable rms force error (less than a few percent). When fewer than five poloidal modes are retained for the high-beta ATF, the rms force error exceeds 15%, even on the finest radial grids. When $m \geq 5$, the force discrepancy drops below 2%, and the flux surfaces attain a characteristic D-shape that is most pronounced in the cross section $\phi = \pi/Q_L$. The convergence of the axis shift, elongation, and D-shape with respect the poloidal mode number and radial mesh is shown in Fig. 13. Note that the extrapolated values for Δ are nearly converged with only three poloidal modes, but elongation and D-shape require at least five modes to converge adequately. In all cases, the radial convergence is nearly quadratic.

Thus, as the plasma pressure increases and the internal flux surface topology becomes more complex, the spectral code will require a broader poloidal spectrum to achieve an adequate representation of the force balance. Such a trend has, indeed, been observed.

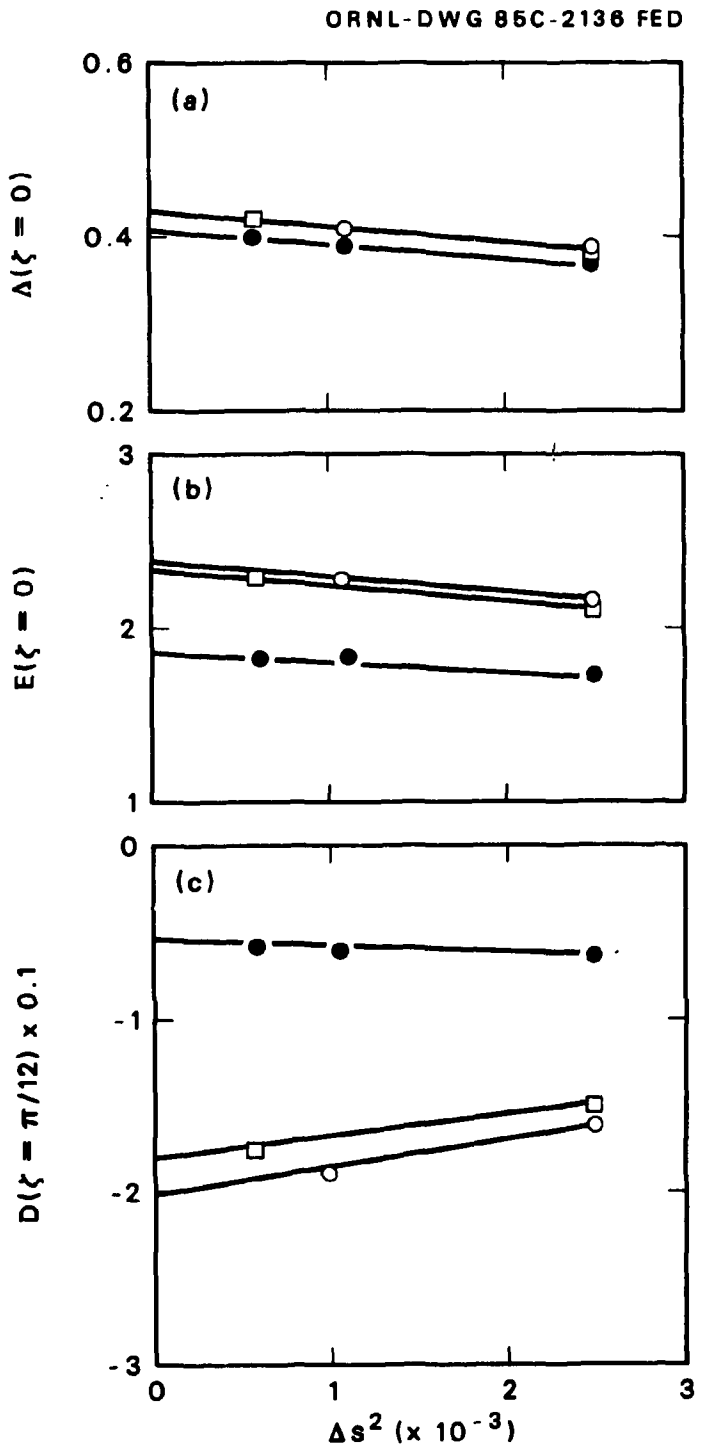

Fig. 13. Radial and mode number convergence studies for shift (Δ), elongation (E), and D-shape (D) for high-beta ATF.

APPENDIX
RESULTS OF CONVERGENCE STUDY

A.1 W7A Vacuum

GRID	$\Delta(0)$		Δ_1^{axis}		W-45	
	BETA	ORMEC	BETA	ORMEC	BETA	ORMEC
15^3	0.027		-0.0005		0.11451	
20^3	0.018	0.0125	0.0025	0.0073	0.11449	0.11449
25^3	0.014	0.0124	0.0042	0.0073	0.11449	0.11449
30^3	0.011	0.0121	0.0052	0.0075	0.11449	0.11448
Extrapolated	0.004	0.0114	0.0075	0.0080	0.11449	0.11448

A.2 Heliotron Vacuum

GRID	$\Delta(0)$		Δ_1^{axis}		W-6	
	BETA	ORMEC	BETA	ORMEC	BETA	ORMEC
15^3	-0.0072		0.0028		.64818	
20^3	-0.0062	-0.0132	0.0031	0.0068	0.64044	0.63105
25^3	-0.0054	-0.0116	0.0033	0.0065	0.63671	0.63066
30^3	-0.0048	-0.0103	0.0034	0.0063	0.63470	0.63045
Extrapolated	-0.0034	-0.0073	0.0036	0.0058	0.63013	0.62997

A.3 Heliotron High-β

GRID	$\Delta(0)$		Δ_1^{axis}		W-6	
	BETA	ORMEC	BETA	ORMEC	BETA	ORMEC
15^3	0.15		-0.028		0.81701	
20^3	0.177	0.128	-0.032	-0.024	0.80903	0.79997
25^3	0.200	0.158	-0.036	-0.030	0.80515	0.79941
30^3	0.218	0.183	-0.039	-0.036	0.80298	0.79902
Extrapolated	0.259	0.239	-0.046	-0.050	0.79804	0.79813

A.4 ATF Vacuum

GRID	$\Delta(0)$		Δ_1^{axis}		W-6	
	BETA	ORMEC	BETA	ORMEC	BETA	ORMEC
15^3	0.205		-0.035		0.64289	
20^3	0.202	0.178	-0.033	-0.019	0.63727	0.62781
25^3	0.203	0.186	-0.033	-0.020	0.63453	0.62754
30^3	0.204	0.192	-0.032	-0.022	0.63299	0.62739
Extrapolated	0.206	0.205	-0.030	-0.027	0.62949	0.62705

A.5 ATF High-β

GRID	$\Delta(0)$		Δ_1^{axis}		W-6	
	BETA	ORMEC	BETA	ORMEC	BETA	ORMEC
15^3	0.361		-0.068		0.80731	
20^3	0.380	0.391	-0.070	-0.073	0.80148	0.7929
25^3	0.396	0.404	-0.074	-0.076	0.79855	0.79206
30^3	0.417	0.413	-0.079	-0.079	0.79676	0.79159
Extrapolated	0.465	0.433	-0.090	-0.086	0.79270	0.79052

REFERENCES

1. S. P. Hirshman and J. C. Whitson, Phys. Fluids 26 (1983), 3553.

2. A. Bhattacharjee, J. C. Wiley, and R. L. Dewar, Comput. Phys. Commun. 31 (1984), 213.

3. L. Lao, Comput. Phys. Commun. 31 (1984), 201.

4. U. Schwenn, Comput. Phys. Commun. 31 (1984), 167.

5. F. Bauer, O. Betancourt, and P. Garabedian, A Computational Method in Plasma Physics, Springer-Verlag, New York, 1978.

6. L. L. Lao, S. P. Hirshman, and R. M. Wieland, Phys. Fluids 24 (1981), 1431.

7. S. P. Hirshman and H. Weitzner, Phys. Fluids 28 (1985), 1207.

8. F. Bauer, O. Betancourt, and P. Garabedian, J. Comput. Phys. 35 (1980), 341.

9. L. S. Solov'ev, Sov. Phys. JETP 26 (1968), 400.

10. K. Ling and S. C. Jardin, J. Comput. Physics (1985), in press.

11. F. Bauer, O. Betancourt, and P. Garabedian, MHD Equilibrium and Stability of Stellarators, Springer-Verlag, New York, 1984.

12. O. Betancourt (private communication). The recommended grid consists of equal angular meshes.

13. F. Hennegger, Z. Naturforsch. 37a (1982), 879.

14. F. Bauer, O. Betancourt, P. Garabedian, and L. Shohet, IEEE Trans. Plasma Sci. PS-9 (1981), 239.

15. J. F. Lyon et al., Proc. 9th Int. Conf. on Plasma Physics and Controlled Nuclear Fusion Research, Baltimore, 1982, IAEA, Vienna, 1983.

16. L. Solov'ev and V. Shafranov, in Reviews of Plasma Physics, ed. by M. A. Leontovich (Consultants Bureau, New York, 1970), Vol. 5, p. 1.

ORNL/TM-9547
Dist. Category UC-20 g

INTERNAL DISTRIBUTION

1. S. E. Attenberger
2. C. O. Beasley
3. B. A. Carreras
4. L. A. Charlton
5. W. A. Cooper
6. E. C. Crume
7. R. A. Dory
8. L. Garcia
9. C. L.Hedrick
10–14. S. P. Hirshman
15–19. J. T. Hogan
20. J. A. Holmes
21. W. A. Houlberg
22. H. C. Howe
23. E. A. Lazarus
24. D. K. Lee
25. J. F. Lyon
26. J. K. Munro
27. G. H. Neilson
28. J. A. Rome
29. M. J. Saltmarsh
30. J. Sheffield
31. J. S. Tolliver
32. W. I. van Rij
33–34. Laboratory Records Department
35. Laboratory Records, ORNL-RC
36. Document Reference Section
37. Central Research Library
38. Fusion Energy Division Library
39–40. Fusion Energy Division Publications Office
41. ORNL Patent Office

EXTERNAL DISTRIBUTION

42. Office of the Assistant Manager for Energy Research and Development, Department of Energy, Oak Ridge Operations Office, P.O. Box E, Oak Ridge, TN 37831
43. J. D. Callen, Department of Nuclear Engineering, University of Wisconsin, Madison, WI 53706
44. R. W. Conn, Department of Chemical, Nuclear, and Thermal Engineering, University of California, Los Angeles, CA 90024
45. S. O. Dean, Director, Fusion Energy Development, Science Applications International Corporation, Gaithersburg, MD 20760
46. H. K. Forsen, Bechtel Group, Inc., Research Engineering, P.O. Box 3965, San Francisco, CA 94105
47. J. R. Gilleland, GA Technologies, Inc., Fusion and Advanced Technology, P.O. Box 85608, San Diego, CA 92138
48. R. W. Gould, Department of Applied Physics, California Institute of Technology, Pasadena, CA 91125
49. R. A. Gross, Plasma Research Laboratory, Columbia University, New York, NY 10027
50. D. M. Meade, Princeton Plasma Physics Laboratory, P.O. Box 451, Princeton, NJ 08544
51. W. M. Stacey, School of Nuclear Engineering, Georgia Institute of Technology, Atlanta, GA 30332
52. D. Steiner, Rensselaer Polytechnic Institute, Troy, NY 12181
53. R. Varma, Physical Research Laboratory, Navrangpura, Ahmedabad 380009, India
54. Bibliothek, Max-Planck Institut fur Plasmaphysik, D-8046 Garching, Federal Republic of Germany

55. Bibliothek, Institut fur Plasmaphysik, KFA, Postfach 1913, D-5170 Julich, Federal Republic of Germany
56. Bibliotheque, Centre des Recherches en Physique des Plasmas, 21 Avenue des Bains, 1007 Lausanne, Switzerland
57. Bibliotheque, Service du Confinement des Plasmas, CEA, B.P. No. 6, 92 Fontenay-aux-Roses (Seine), France
58. Documentation S.I.G.N., Departement de la Physique du Plasma et de la Fusion Controlee, Centre d'Etudes Nucleaires, B.P. 85, Centre du Tri, 38081 Cedex, Grenoble, France
59. Library, Culham Laboratory, UKAEA, Abingdon, Oxfordshire, OX14 3DB, England
60. Library, FOM-Instituut voor Plasma-Fysica, Rijnhuizen, Edisonbaan 14, 3439 MN Nieuwegein, The Netherlands
61. Library, Institute of Plasma Physics, Nagoya University, Nagoya, Japan
62. Library, International Centre for Theoretical Physics, Trieste, Italy
63. Library, Laboratorio Gas Ionizatti, CP 56, I-00044 Frascati, Rome, Italy
64. Library, Plasma Physics Laboratory, Kyoto University, Gokasho, Uji, Kyoto, Japan
65. Plasma Research Laboratory, Australian National University, P.O. Box 4, Canberra, A.C.T. 2000, Australia
66. Thermonuclear Library, Japan Atomic Energy Research Institute, Tokai, Naka, Ibaraki, Japan
67. G. A. Eliseev, I. V. Kurchatov Institute of Atomic Energy, P.O. Box 3402, 123182 Moscow, U.S.S.R.
68. V. A. Glukhikh, Scientific-Research Institute of Electro-Physical Apparatus, 188631 Leningrad, U.S.S.R.
69. I. Shpigel, Lebedev Physical Institute, Leninsky Prospect 53, 117924 Moscow, U.S.S.R.
70. D. D. Ryutov, Institute of Nuclear Physics, Siberian Branch of the Academy of Sciences of the U.S.S.R., Sovetskaya St. 5, 630090 Novosibirsk, U.S.S.R.
71. V. T. Tolok, Kharkov Physical-Technical Institute, Academical St. 1, 310108 Kharkov, U.S.S.R.
72. Library, Institute of Physics, Academia Sinica, Beijing, Peoples' Republic of China
73. J. F. Clarke, Associate Director for Fusion Energy, Office of Energy Research, ER-50, Germantown, U.S. Department of Energy, Washington, DC 20545
74. W. Sadowski, Fusion Theory and Computer Services Branch, Office of Fusion Energy, Office of Energy Research, ER-541, Germantown, U.S. Department of Energy, Washington, DC 20545
75. N. A. Davies, Office of the Associate Director, Office of Fusion Energy, Office of Energy Research, ER-51, Germantown, U.S. Department of Energy, Washington, DC 20545
76. E. Oktay, Division of Confinement Systems, Office of Fusion Energy, Office of Energy Research, ER-55, Germantown, U.S. Department of Energy, Washington, DC 20545
77. M. N. Rosenbluth, Institute for Fusion Studies, University of Texas, RLM 11.218, Austin, TX 78712
78. Theory Department Read File, c/o D. W. Ross, Institute for Fusion Studies, University of Texas, Austin, TX 78712
79. Theory Department Read File, c/o R. C. Davidson, Director, Plasma Fusion Center, NW 16-202, Massachusetts Institute of Technology, Cambridge, MA 02139
80. Theory Department Read File, c/o F. W. Perkins, Princeton Plasma Physics Laboratory, P.O. Box 451, Princeton, NJ 08544
81. Theory Department Read File, c/o L. Kovrizhnykh, Lebedev Institute of Physics, Academy of Sciences, 53 Leninsky Prospect, 117924 Moscow, U.S.S.R.
82. Theory Department Read File, c/o B. B. Kadomtsev, I. V. Kurchatov Institute of Atomic Energy, P.O. Box 3402, 123182 Moscow, U.S.S.R.
83. Theory Department Read File, c/o T. Kamimura, Institute of Plasma Physics, Nagoya University, Nagoya, Japan

84. Theory Department Read File, c/o C. Mercier, Euratom-CEA, Service des Recherches sur la Fusion Controlee, Fontenay-aux-Roses (Seine), France
85. Theory Department Read File, c/o T. E. Stringer, JET Joint Undertaking, Culham Laboratory, Abingdon, Oxfordshire OX14 3DB, England
86. Theory Department Read File, c/o K. Roberts, Culham Laboratory, Abingdon, Oxfordshire OX14 3DB, England
87. Theory Department Read File, c/o D. Biskamp, Max-Planck-Institut fur Plasmaphysik, D-8046 Garching, Federal Republic of Germany
88. Theory Department Read File, c/o T. Takeda, Japan Atomic Energy Research Institute, Tokai, Naka, Ibaraki, Japan
89. Theory Department Read File, c/o C. S. Liu, GA Technologies, Inc., P.O. Box 81608, San Diego, CA 92138
90. Theory Department Read File, c/o L. D. Pearlstein, Lawrence Livermore National Laboratory, P.O. Box 808, Livermore, CA 94550
91. Theory Department Read File, c/o R. Gerwin, CTR Division, Los Alamos National Laboratory, P.O. Box 1663, Los Alamos, NM 87545
92. R. E. Mickens, Department of Physics, Atlanta University, Atlanta, GA 30314
93. G. Bateman, Princeton Plasma Physics Laboratory, P.O. Box 451, Princeton, NJ 08544
94. I. Bernstein, Yale University, New Haven, CT 06520
95. A. Bers, 38-260, Massachusetts Institute of Technology, Cambridge, MA 02139
96. O. Betancourt, Courant Institute of Mathematical Sciences, New York University, 251 Mercer Street, New York, NY 10012
97. A. Bhattacharjee, Columbia University, New York, NY 10027
98. H. H. Chen, Physics Department, University of Maryland, College Park, MD 20742
99. L. Chen, Princeton Plasma Physics Laboratory, P.O. Box 451, Princeton, NJ 08544
100. J. Cordey, Culham Laboratory, UKAEA Research Group, Abingdon, Oxfordshire OX14 3DB, England
101. J. DeLucia, Princeton Plasma Physics Laboratory, P.O. Box 451, Princeton, NJ 08544
102. P. Garabedian, Courant Institute of Mathematical Sciences, New York University, 251 Mercer Street, New York, NY 10012
103. A. Glasser, Los Alamos National Laboratory, Los Alamos, NM 87545
104. H. Goedbloed, Plasma Fusion Center, NW 16-243, Massachusetts Institute of Technology, Cambridge, MA 02139
105. H. Grad, Magnets-Fluid Dynamics Division, Courant Institute of Mathematical Sciences, New York University, 251 Mercer Street, New York, NY 10012
106. J. M. Greene, GA Technologies, Inc., San Diego, CA 92138
107. L. Hall, L-630, Lawrence Livermore National Laboratory, P.O. Box 5511, Livermore, CA 94550
108. L. Ibanez, Courant Institute of Mathematical Sciences, New York University, 251 Mercer Street, New York, NY 10012
109. S. C. Jardin, Princeton Plasma Physics Laboratory, P.O. Box 451, Princeton, NJ 08544
110. W. Kerner, Courant Institute of Mathematical Sciences, New York University, 251 Mercer Street, New York, NY 10012
111. L. L. Lao, TO-512, GA Technologies, Inc., San Diego, CA 92138
112. K. M. Liang, Los Alamos National Laboratory, Los Alamos, NM 87545
113. R. McCall, Princeton Plasma Physics Laboratory, P.O. Box 451, Princeton, NJ 08544
114. B. Miner, Science Applications International Corporation, 1710 Goodridge Drive, McLean, VA 22102
115. R. W. Moses, MS 642, Los Alamos National Laboratory, Los Alamos, NM 87545
116. H. Mynick, ECE Department, Princeton Plasma Physics Laboratory, Princeton, NJ 08544

117. J. Nuhrenberg, Max Planck Institute for Plasma Physics, D-8046 Garching, Federal Republic of Germany
118. N. Pomphrey, Princeton Plasma Physics Laboratory, P.O. Box 451, Princeton, NJ 08544
119. A. Riedel, Courant Institute of Mathematical Sciences, New York University, 251 Mercer Street, New York, NY 10012
120. P. H. Rutherford, Princeton Plasma Physics Laboratory, P.O. Box 451, Princeton, NJ 08544
121. A. G. Sgro, Los Alamos National Laboratory, Los Alamos, NM 87545
122. A. Schluter, Max-Planck Institut fur Plasma Physik, D-8046 Garching, Federal Republic of Germany
123. U. Schwenn, Max-Planck Institut fur Plasma Physik, D-8046 Garching, Federal Republic of Germany
124. V. D. Shafranov, I. V. Kurchatov Institute of Atomic Energy, P.O. Box 3042, 123182 Moscow, U.S.S.R.
125. J. L. Shohet, Stellarator-Torsatron Laboratory, University of Wisconsin, Madison, WI 53706
126. A. M. M. Todd, Grumman Aerospace Corporation, 105 College Road East, Princeton, NJ 08540
127. Y. M. Treve, 125 San Rafael Avenue, Santa Barbara, CA 93109
128. J. W. Van Dam, Institute for Fusion Studies, RLM.222, University of Texas, Austin, TX 78712
129. H. Weitzner, Courant Institute of Mathematical Sciences, New York University, 251 Mercer Street, New York, NY 10012
130. J. C. Wiley, Institute for Fusion Studies, RLM 11.222, University of Texas, Austin, TX 78712

131–286. Given distribution according to TIC-4500, Magnetic Fusion Energy (Distribution Category UC-20 g: Theoretical Plasma Physics)

6. CONCLUSIONS

The spectral inverse method has been shown to be an efficient means for computing accurate and realistic 3-D equilibria. Previous estimates[1-4] for the improvement in computational efficiency effected by spectral methods compared with difference methods ranged from one to two orders of magnitude. For complex boundaries, the present study finds a much smaller discrepancy between the overall efficiency of the two inverse methods, especially when stringent error tolerances require the presence of many spectral modes.

Quadratic dependence on the radial mesh spacing Δs of the energy, toroidal shift, and helical axis shift has been demonstrated for the ORMEC spectral code. Scalings for the axis shift and helical axis computed from BETA seem to lie between Δs and Δs^2, as previously noted in Ref. 5, with the quadratic dependence of the energy emerging as the only indisputable scaling.